Chapter 6

Low Temperature Hybrid Processing Technology of Fine Electronic Ceramics

Hongfang Zhang, Chee-leung Mak,
Helen Lai-Wa Chan and Xi Yao

Additional information is available at the end of the chapter

http://dx.doi.org/10.5772/53255

1. Introduction

Low temperature sintering is of vital importance for commercial production of electronic ceramics, especially multi-layer devices [1, 2]. Due to superior mechanical strength, ferroelectric ceramics with fine-grained structures have attracted much attention and exhibited potential applications such as piezoelectric sensors and actuators [3, 4-5]. Together, composite materials are also widely applied for multilayer capacitors, piezoelectric transducers, packaging materials for integrated circuits, high voltage insulators and chemical sensors [6-10]. It is well known that materials' performances are closely related to the ways they are manufactured. Generally, ferroelectric ceramics fabrication process should achieve products of dense and homogeneous microstructure with well developed crystalline grains of uniform size in order to ensure the best physical properties. Using conventional ceramic process to achieve such ideal microstructure, the window of sintering temperature required is always high and narrow. Conversely, the sintering temperature of sol-gel derived ceramics is always lower. However, the drawbacks of sol–gel method are aggregation of ultrafine powders during fabrication and formation of secondary phases [11]. Thus, the physical properties of these sol-gel derived ceramics are deteriorated in comparison to those of their counterparts. Recently, dense, crack-free ferroelectric thick film integrated on silicon substrate has been the subject of considerable attention for potential application in micro-electro-mechanical systems (MEMS). Combining micro-machined surfaces of silicon wafers with ferroelectric films has resulted in novel devices such as micro-fluidic devices, micro-pumps, infrared sensors, dynamic random access memory, tunable microwave devices and several others [12-16]. Most of these ferroelectric thick film devices, such as multi-layer ceramic capacitors (MLCC), require the film thickness to be around 1 micrometer. In addition, these

devices need to be co-fired with less expensive base metal electrode at low temperature. Therefore, the existing technology can no longer meet such requirements. Many attempts have been devoted to develop new technologies to meet these new technological challenges. Indeed, a new hybrid ceramic processing technology has been developed [17-22]. The key characteristic of this new technology is to graft the sol-gel wet chemistry process onto the conventional mixed oxide ceramic process. With this new technology, the advantages of both processes can be superimposed together. The good performance of ceramics prepared by conventional ceramic process under high temperatures is mostly preserved, while the sintering temperature of the devices is effectively reduced down as inherited from the sol-gel process. The low sintering temperature of this hybrid process enables the technology better compatible to the thick film technology. Low sintering temperature also impedes the chemical reactions among different materials in the devices, such as ceramic/electrode, ceramic/substrate and ceramics/matrix. This new technology will be very useful in developing all-ceramics devices such as microwave barium-strontium titanate ($Ba_{0.6}Sr_{0.4}TiO_3$, BST) ceramics, thick films and composite materials. This chapter reviews our recent progress in the synthesis of various ferroelectric ceramic materials and composites via the proposed hybrid process. After the background introduction, a brief description of the experimental procedures is followed. In Section 3, synthesis processes and characterization of various ferroelectric ceramics and composites are presented. Finally, the chapter is ended with some concluding remarks.

2. Features of the low temperature hybrid processing route

Figure 1 is the schematic diagram illustrating the entire formation process of a representative microwave BST thick film.

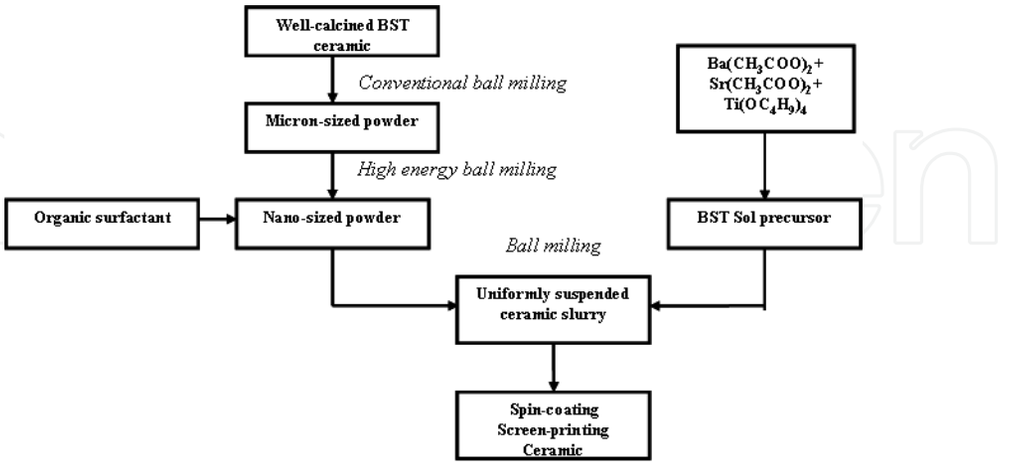

Figure 1. Flow chat of the hybrid processing of a typical microwave BST thick film.

As shown in Fig. 1, this processing route is quite flexible. Changing the process parameters of ball milling (i.e. conventional as well as high energy) such as revolution speed and ball

http://dx.doi.org/10.5772/53255

milling time, the particle size can be easily controlled. On the other hand, the thickness of the film can be increased by repeating the spin-coating or screen-printing process. In addition, the viscosity of the ceramic slurry can be adjusted by altering the powder/sol ratio as well as the amount of organic solvent. In fact, the viscosity of the slurry affects the film thickness for each spin-coating/screen-printing layer. For calcinated sol-gel precursor possessing the same composition as that of the nano-sized powders, the mixture obtained is a homogenous mixture, and the resulting composite has single composition. In contrast, if the precursor solution and the nano-powders are of different compositions, multiphase composite will be produced forming a heterogeneous composite. Using this method, uniformly distributed multiphase nanocrystalline composite can be obtained easily. The composite normally exhibits all the merits of the nano-powders and the sol-gel precursor. We can find different applications of this route by utilizing its respective merits. For example, by using uniformly dispersed nano-powders in sol-gel solution we demonstrated that homogeneous thick films were obtained by spin coating technique [20, 22]. Using sol-gel precursor as binder, the density of the compacted films was increased and the sintering temperature of the compacted films was reduced. Similar, for screen-printing films, low sintering temperature will be expected. This unique feature is particularly useful to low temperature co-firing of multilayer devices because cheap internal electrode paste can be used. We consider that the simplicity of this approach should make it useful to most of the ceramic processes.

3. Formation and characterization of fine ferroelectric and composite electroceramics via hybrid process

3.1. Microwave fine-grained BST and BST-MgO ceramics

3.1.1. Fine-grained BST ceramics

3.1.1.1. Sintering behavior

In Fig. 1, pre-calcined BST powders were firstly prepared by a conventional ceramic process using commercial $BaTiO_3$ (BT) powder of mean grain size smaller than 400 nm, and $SrTiO_3$ (ST) powder of size smaller than 100 nm. The powders were mixed together by using conventional ball milling for 2 h and then calcined at 1150°C for 2 h to form the BST ceramics. Then, the BST ceramics were ball milled by a normal planetary ball mill machine with zirconia balls as the milling medium. The size of the obtained powder particle was around few micrometers to sub-micrometers. Afterwards, a high-energy ball-milling machine (Frisch Pulverisette 5 planetary ball-milling machine, Germany) with a tungsten carbide milling jar and milling medium was used to prepare the nano-sized powders. The size of the final powder was in the range of 20–60 nm depending on the process parameters. During the course of high-energy ball milling, a selected dispersant was added to the nano-powder to prevent the agglomeration of the nano-sized powder. On the other hand, BST sol precursor in the same chemical composition as the powder was synthesized via a

polymer-assistant sol-gel route. Here the starting materials for the sol precursor were $Ba(CH_3COO)_2$, $Sr(CH_3COO)_2$ and $Ti(OC_2H_5)_4$. The details of the fabrication process can be found elsewhere [20]. To graft the sol gel process onto the conventional ceramic process, pre-synthesized BST sol was mixed with BST nano-sized powder by conventional ball milling. Due to the effect of the organic surfactant used, the BST powder was well dispersed and suspended in the BST sol solution forming uniform paint-like ceramic slurry. In this hybrid process, the molar ratio of BST introduced in the form of powder and in the form of sol solution was very important. In the current investigation, an optimized mass ratio of ceramic powder/sol precursor equivalent to 72/28 was adopted. For preparing bulk ceramics, the as-prepared ceramic slurry was dried at 120~150°C and then calcined at 800~1000°C for 2 h. Then calcined powder was uniaxially pressed at 4 MPa to form a green BST compact which was heated to 1200°C for 2 h, with a heating rate of 2°C/min in air. For comparison, coarse-grained BST ceramics were prepared by a conventional solid-state reaction method from the pre-calcined micron-sized BST powders (i.e. the powders calcined at 1150°C) at a sintering temperature of 1400 °C for 2 h in air.

3.1.1.2. Microstructure and properties

Figure 2 shows the X-ray diffraction patterns of (a) commercial BT powder, (b) commercial ST powder, (c) coarse-grained BST ceramics fabricated by conventional solid-state reaction method and sintered at 1400°C, and (d) BST ceramics fabricated by hybrid process technology and sintered at 1200°C. In Figs. 2(a) and (b), the XRD patterns show that the BT and ST powders are in tetragonal and cubic phase, respectively. Figs. 2(c) and (d) indicate the presence of highly pure and crystalline pervoskite cubic structure. All the peaks were identified as BST phase and no impurity phase was observed, indicating the success in synthesizing BST ceramics by the two processing routes.

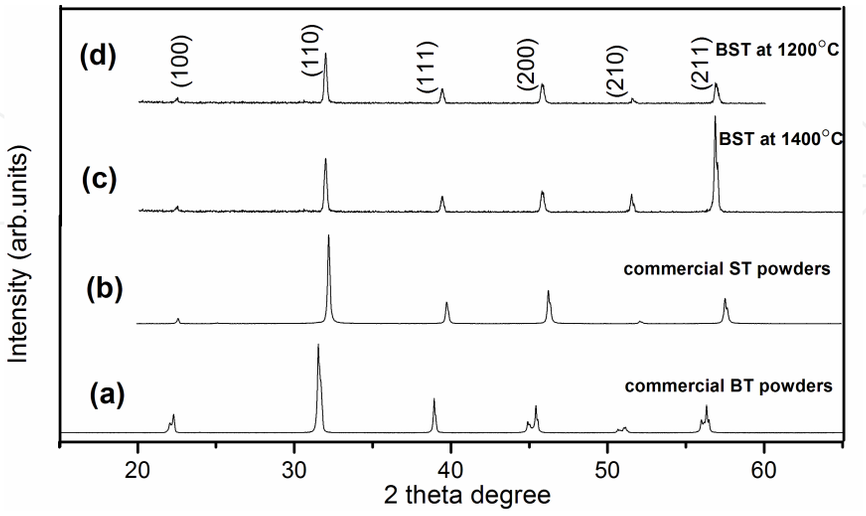

Figure 2. X-ray diffraction (XRD) patterns: (a) and (b) commercial BaTiO3 and SrTiO3 powders; and BST ceramics sintered at (c) 1400°C using conventional solid-state process, (d) 1200°C using hybrid process.

http://dx.doi.org/10.5772/53255

Figure 3 shows the SEM images of (a) coarse-grained BST ceramics fabricated by conventional solid-state reaction method, and (b) fine-grained BST ceramics fabricated by hybrid process technology. The images showed that both ceramics possessed well-densified grains of various size and shape. In general, the grains size in Fig. 3(a) was larger than those in Fig. 3(b) and the grain size ranges were 5-10 μm and 1-2 μm for Figs. 3(a) and (b), respectively. It is noticed that the fine-grained ceramic fabricated by the hybrid process was densified at a sintering temperature 200°C lower than that of the conventional solid-state process. The lower sintering temperature of the hybrid process is most inherited from the low crystallization and sintering temperature of the amorphous gel components of the hybrid BST powder. Sol-gel process is usually characterized with much lower sintering temperature because of higher chemical reactivity and shorter diffusion length [23]. On the other hand, the BST gel solution acts as binding agent to connect the nano-sized BST particles and fills the interstitials of the nano-sized particles, which is easy to achieve dramatic modification of the processing behaviors of ceramics, and useful to produce uniform and fine-grained high-quality ceramics at low sintering temperatures.

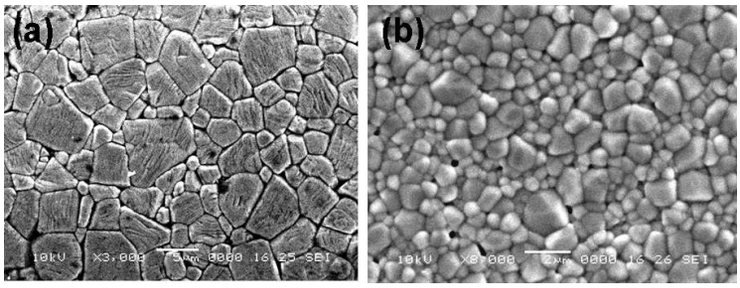

Figure 3. Surface morphology of BST ceramics by (a) the conventional solid-state process at 1400°C, and (b) by the hybrid process at 1200 °C.

The corresponding temperature dependency of dielectric constant and loss tangent for BST ceramic prepared by conventional solid-state process and hybrid process are shown in Figure 4. As shown in Fig. 4(a), for the coarse-grained BST ceramic, the peak dielectric constant at 10 kHz was around 6500 with a loss tangent about 0.02. Though the dielectric constant in coarse-grained ceramic was high due to the well-developed large grains; however, the grain size was too large and the grain size distribution was too large so that the microstructure was not very uniform as required in many applications. In Fig. 4(b), for the fine-grained BST ceramic, a broader and diffused peak was observed in both the dielectric constant and loss tangent spectra indicating the characteristic dispersion at the Curie point. The peak dielectric constant was about 2500 at 10 kHz with a loss tangent about 0.02. The peak dielectric constant is lower than that of the conventional solid-state process mostly due to the finer structure.

The dielectric tunability, defined as the change of dielectric constant in the presence of a dc electric field with respect to the dielectric constant in the absence of a dc electric field, is shown in Figure 5. The tunability of the fine-grained BST ceramic was found to be about 36% at 11 kV/cm at room temperature, the dielectric loss was in the range of 10^{-2}.

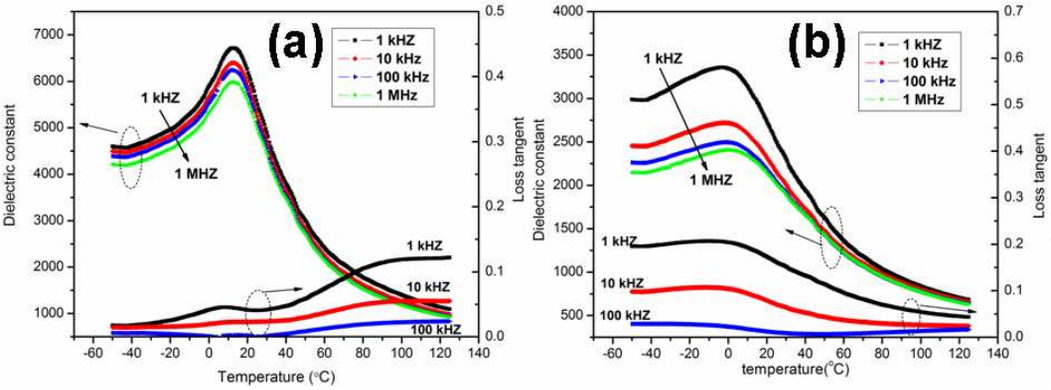

Figure 4. Temperature dependences of dielectric constant and loss tangent for BST ceramic via (a) conventional ceramic process, and (b) hybrid processing.

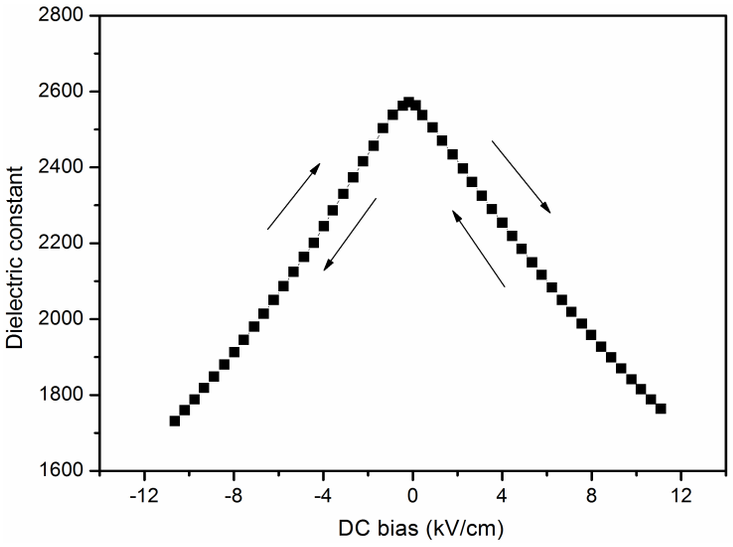

Figure 5. Tuning behavior of dielectric constant of fine-grained BST ceramic at 10 kHz and room temperature under DC bias voltage.

3.1.2. Fine-grained BST-MgO ceramics

3.1.2.1. Sintering behavior

To fabricate BST-MgO ceramics, the same BST ceramic slurry described in Section 3.1.1.1 was employed. Magnesium nitrate hexahydrate ($Mg(NO_3).6H_2O$) solution was added to the BST slurry, then subjected to a conventional ball-milling for 2h to obtain heterogenous BST-MgO ceramic slurry. The paint-like BST-MgO slurry was dried at 120°C, and then calcined at 800°C for 4h. The pre-calcined powder was uniaxially pressed into disk pellets at a pressure of 4 MPa in a stainless steel die. The pressed pellets were sintered in air at 1200–1300°C for 2h.

http://dx.doi.org/10.5772/53255

3.1.2.2. Microstructure and properties

Figure 6 shows the XRD patterns of (a) the nano-sized BST powders, (b) BST-MgO slurry dried at 120°C, (c) BST-MgO slurry calcined at 800°C for 4h, (d) BST-MgO ceramics sintered at 1200°C for 2h, and (e) BST-MgO ceramics sintered at 1300°C for 2h. The XRD pattern in Fig. 6(a) suggested the presence of BST powder of pure perovskite structure. The XRD pattern of the dried BST-MgO slurry in Fig. 6(b) only displayed the peaks of the BST powder and no MgO peaks were observed, indicating that the MgO was still in an amorphous phase and there was no chemical reaction between the BST and MgO phases. It is seen from Figs. 6(c)–(e) that the BST and MgO phases coexisted in both the calcined BST-MgO slurry and the sintered BST-MgO ceramics, and all the XRD peaks corresponding to both the BST and MgO phases were identified with no detection of intermediate or interfacial phases. The results indicate the success in synthesizing BST-MgO ceramics using the hybrid processing route.

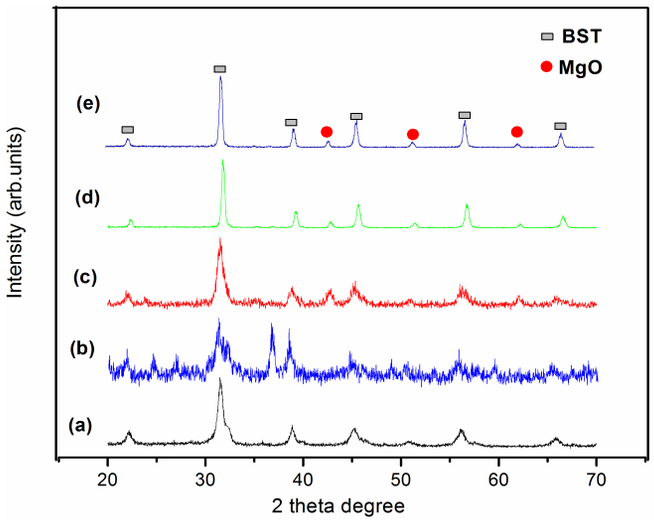

Figure 6. XRD patterns of (a) BST powders, (b) BST-MgO slurry dried at 120°C, (c) BST-MgO slurry calcined at 800°C for 4h, (d) BST-MgO ceramics sintered at 1200°C for 2h, and (e) BST-MgO ceramics sintered at 1300°C for 2h.

Figure 7 illustrates the SEM images of BST-MgO ceramics sintered at three different temperatures ranging between 1200 and 1300°C for 2 h via hybrid processing. It is noticed that densification of the ceramic was taken place at 1200°C with grain size of about 300 nm. With increasing sintering temperature to 1275~1300°C, the ceramics were further densified with grain size increased to about 1–2 μm, and no apparent grain growth was observed after 1275°C. Thus, dense, homogeneous and fine-crystalline BST-MgO ceramics were produced at sintering temperatures below 1300°C. It has been reported [24] that sintering temperature in the range of 1350–1500°C was indispensable in the fabrication of BST-MgO ceramics using conventional solid-state process. This high sintering temperature resulted in large grains as well as pores, and followed by the deterioration of microstructures as well as properties of the resulting ceramics. Fortunately, such phenomena were not evident in our BST-MgO ceramics synthesized by the hybrid processing route. As shown in Fig. 7, sintering temperature of 1200°C was good enough for the synthesis of BST-MgO ceramics with a reasonably

high density of 4.50 g/cm^3. We attribute these promising results to the characteristics of the hybrid processing route as mentioned above. Besides, the sol–gel derived species can act as the buffer for another phase inhibiting the grain size in the sub-micron scale.

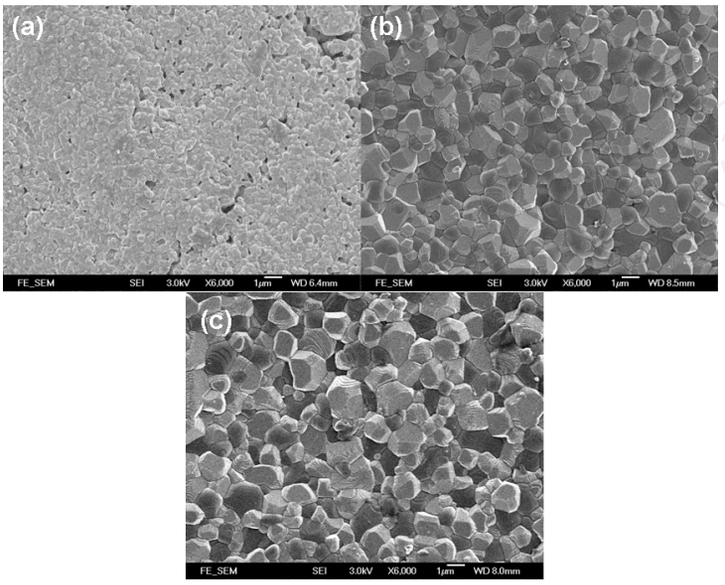

Figure 7. The surface morphologies of BST composite bulk ceramics sintered at (a) 1200°C ; (b) 1275°C; (b) 1300°C for 2 h via the hybrid process. Note: the EDX results suggested that grains with light color corresponded to the BST phase while grains with dark color were MgO phase.

Figure 8 shows the temperature dependency of the relative dielectric constant ε_r and loss tangent (tan δ) in the temperature range of -60°C to 80°C for three selected frequencies (1 kHz, 10 kHz, and 100 kHz). A relatively broad and diffused phase transition was clearly identified at about -20°C for both samples. The ceramics demonstrated very low room temperature loss tangent below 0.005 for frequency above 1 kHz. Reduced temperature variation of dielectric properties in these samples is desirable for application of the ceramics in electrically tunable microwave devices to improve their temperature and frequency stabilities [25].

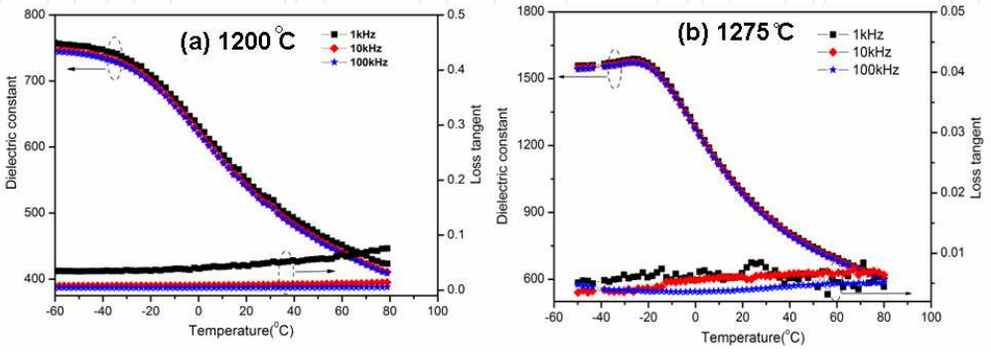

Figure 8. Temperature dependences of dielectric constant and loss tangent for the BST-MgO ceramics sintered at 1200 and 1275°C via hybrid process.

http://dx.doi.org/10.5772/53255

To explore the application of the ceramics in microwave devices, dc electric field was employed to change the dielectric constant of the BST-MgO ceramics. Figure 9 shows the room temperature dielectric constant as a function of dc electric field for BST-MgO ceramics sintered at 1200°C and 1300°C with average grain sizes of 300 nm and 2 μm at 100 kHz respectively. The dielectric tunability was found to be 4% and 14% respectively, under a dc electric field of 1.5 kV/mm.

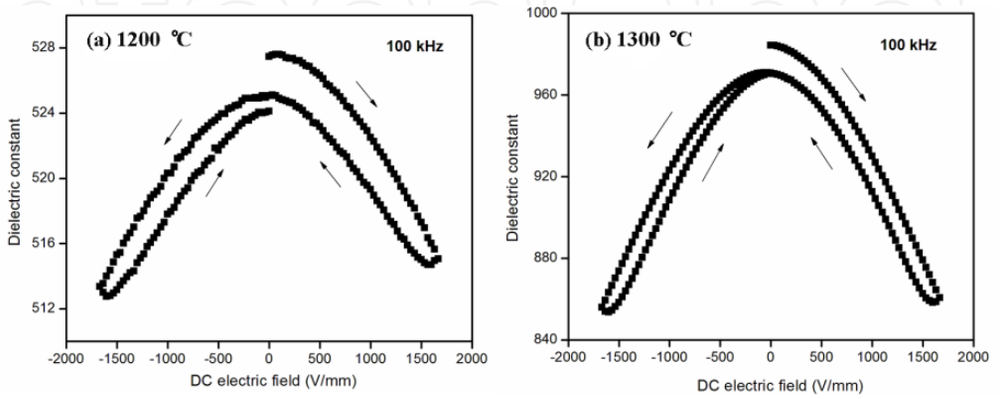

Figure 9. Room-temperature dielectric constant as a function of dc electric field for the ceramics sintered at 1200 and 1300°C at 100 kHz.

3.2. Microwave BST ceramic thick films

3.2.1. Sintering behavior

As shown in Fig. 1, the BST powder, being acted as filler in the BST ceramic slurry, plays an important role in the formation of dense and crack free films. It also strongly affects the surface morphology and resultant properties of the thick films. Therefore, well-crystallized nano-size or micron-size BST ceramic powders or their combinations, which had been presintered at 1350°C for 7 h using conventional solid-state ceramic process, were dispersed into BST sol precursor to form uniformly suspended BST ceramic slurry. The BST ceramic slurry was spin-coated onto Pt substrates or Ag/alumina substrates at a spin rate of 3000 rpm for 20 s. The optimum thickness of a single deposition layer was about 1–2 μm. Thicker films were obtained by repeating the spin-coating process. For thick film deposition, the weight ratio of powder to precursor solution of the slurry was a critical parameter. The *wt%* BST powder in the ceramic slurry is defined as:

$$BST(wt\%) = \frac{p}{p+s} \tag{1}$$

where $p$is the weight of BST powder added, $s$is the residue oxide weight of the BST sol solution after thermal annealing. On the basis of our results, the optimal BST ($wt\%$) was between 70 and 80% in order to get the maximum thickness in a crack-free layer using one spin-coat-

ing process. In the experiment, the viscosity of the slurry was controlled by adjusting the amount of organic solvent. The as-deposited films were calcined at about 550°C to remove all organic solvent. Afterwards, the films were densified at a higher temperature of around 600–900°C, depending on the electrode used. The paste for screen printing was prepared by the following processing route: first, the ceramic slurry was calcined in order to remove solvents as well as organics brought in by the sol solution. The calcined powder was dispersed into an organic vehicle specifically designed for screen-printing. Green films were printed on Pd–Ag-electroded alumina substrates by screen-printing. The thickness of each single layer was about 5–10 μm depending on the loading percentage of the ceramic powder and the viscosity of the printing paste. In order to obtain thick films, the printing process was repeated. Each layer of the screen-printed wet film was allowed to settle at room temperature for 15 min and dried in an oven at 120°C for another 15 min. The final films were sintered at temperatures of around 1200°C for 2 h.

3.2.2. Microstructure and properties

Figure 10 shows the X-ray diffraction patterns of BST thick film deposited on different substrates annealed at different temperatures. It is quite evident that the crystal structures of the films were of cubic perovskite structure. Besides the diffraction peaks arisen from BST phase as well as the Pt substrate or silver electrodes and alumina substrates, no other impurity phases were observed.

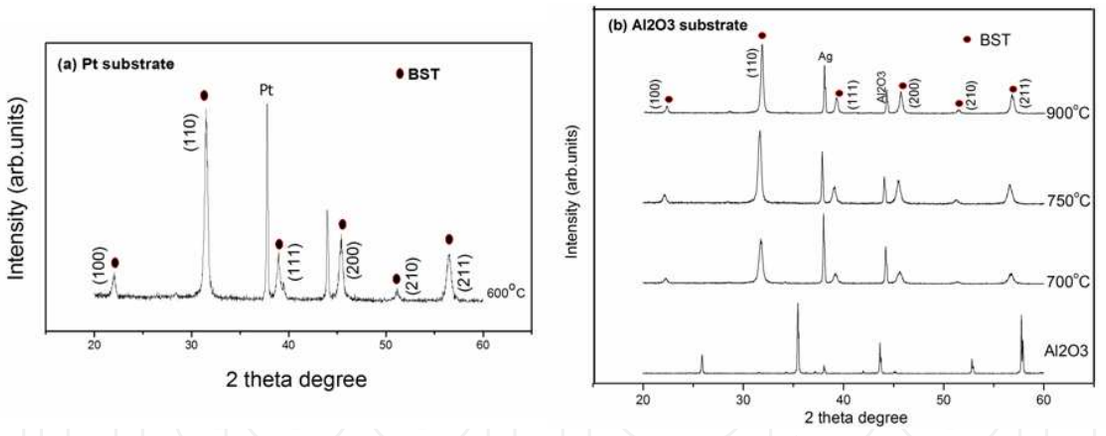

Figure 10. X-Ray diffraction patterns of BST thick films with various calcining temperatures deposited on either Pt or Ag/alumina substrates.

Figure 11 displays the SEM pictures of the surface (Figs. 11(a) and (c)) and the cross-section (Figs. 11(b) and (d)) of the BST thick films deposited on various substrates. It is noticed that the films were, in general, dense, uniform and crack-free. In Fig. 11 (b), the film, with only single deposited layer, had a film thickness over 1 μm. On the other hand, in Fig. 11(d), the film, with 10 deposited layers in totally, had a film thickness of about 10 μm. Thus, the average thickness for one coated layer was estimated to be about 1 μm, similar to that observed in Fig. 11(b). The sol-gel derived phase, shown as crystallites between the granular grains,

http://dx.doi.org/10.5772/53255

was clearly seen in the microstructure. This sol-gel derived phase acted as a binder for the granular grains and filled the interstitials of the added powders. The agglomeration, which easily exists in conventional sol-gel derived ceramics and nanocomposite route, was not observed in Figs. 11. Therefore, we believe that agglomeration was eliminated by the hybrid process, demonstrating the advantage of this novel route.

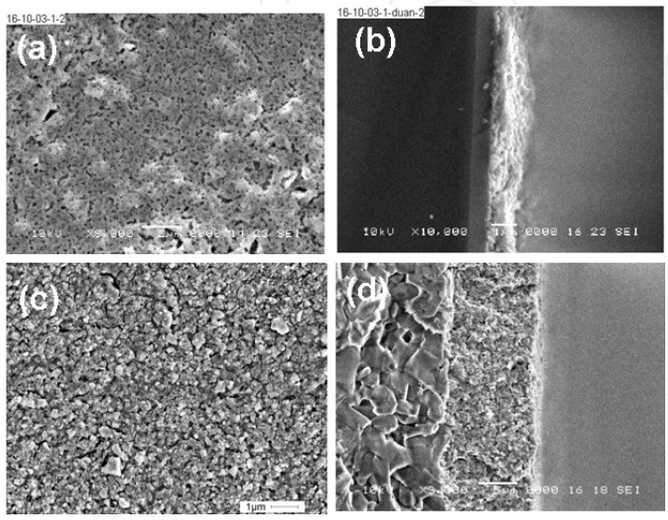

Figure 11. The surface and cross-sectional morphologies of thick films prepared from the slurry using the spin-coating method deposited on Pt substrates with one layer and Ag/alumina with 10 layers annealed at 600 and 700°C, respectively.

Figure 12 shows the temperature dependence relative dielectric constant ε_r and loss tangent (tan δ) for BST thick films deposited on (a) Pt substrate annealed at 600°C, and (b)−(d) Ag/alumina substrates annealed at 700, 750 and 900°C respectively, in the temperature range of -35°C to 120°C for four selected frequencies (1 kHz, 10 kHz, 100 kHz and 1 MHz). A relatively broad phase transition was clearly identified at about 0°C for all samples. With increasing annealing temperature, the dielectric constant increased gradually. For example, at 10 kHz at zero temperature, the dielectric constant of the thick films deposited on Pt substrate (Fig. 12(a)) was found to be about 150 with a loss tangent slightly below 0.02, for the thick films deposited on Ag/alumina substrates annealed at 900°C, the dielectric constant (Fig.12(d)) was about 370 with a loss tangent slightly below 0.01.

Figure 13 illustrates the room temperature tuning behavior of the BST thick films deposited on (a) Pt substrate annealed at 600°C, and (b)−(c) Ag/alumina substrates annealed at 750 and 900°C respectively at 100 kHz and under dc bias voltage. In Fig. 13(a), the room temperature dielectric constant at zero bias condition varied between 160 and 135, while the tunability of the dielectric constant of the thick film changed from 12% at 60 kV/cm with a loss tangent of about 0.015 to about 30% at 35 kV/cm with a loss tangent of 0.0067 (as shown in Fig. 13(b)). In Fig. 13(c) the tunability was 28% at 20 kV/cm with a loss tangent of 0.008. Usually, thick films with higher dielectric constants possess higher tunability of dielectric constant but poorer temperature stability [20]. General speaking, reducing the dielectric constant of the film will reduce its tunability but improve its temperature stability.

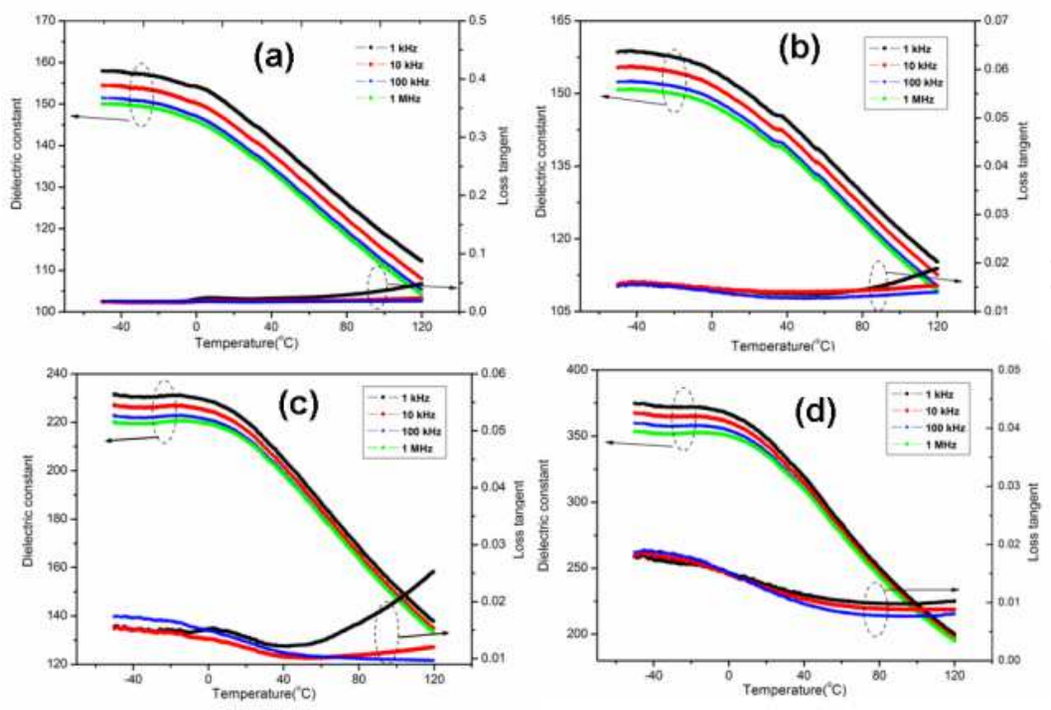

Figure 12. Temperature dependence dielectric constant and loss tangent for BST thick films deposited on (a) Pt substrate annealed at 600°C, (b) –(d) Ag/alumina substrates annealed at 700, 750 and 900°C, respectively.

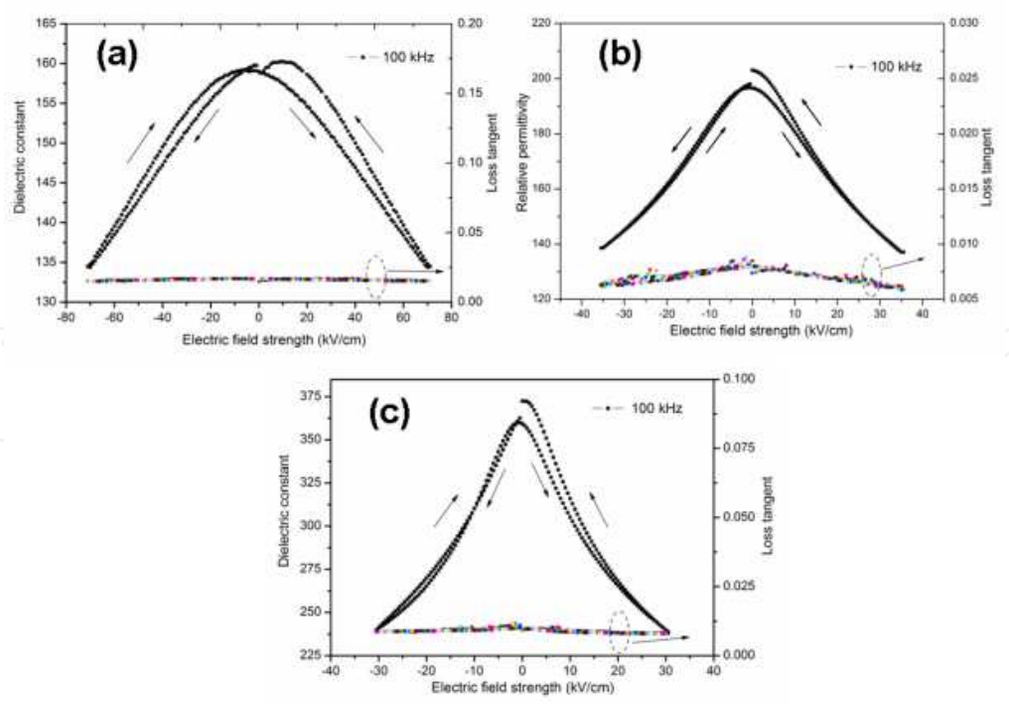

Figure 13. dc bias voltage dependency of the dielectric constant and loss tangent of thick BST films deposited on (a) Pt substrate annealed at 600°C, (b)–(c) Ag/alumina substrates annealed at 750 and 900°C respectively at 25°C.

http://dx.doi.org/10.5772/53255

The effects of the BST powder as filler in the sol precursor on the structural as well as dielectric properties of BST thick films prepared by screen-printing method were also investigated. One is the ceramic slurry was prepared by dispersing nano-sized BST powder in the BST sol precursor. Figure 14 shows the (a) XRD pattern, (b) surface and (c) cross-section micrographs of BST thick films deposited on Pd-Ag/ alumina substrate by screen-printing method. The films were sintered at 1200°C in air. As shown in Fig. 14(a), XRD pattern exhibited a pure BST perovskite structure in cubic phase with no observable intermediate as well as impurity phases, except the diffraction peaks arisen from Pd-Ag electrode and alumina substrate. As observed in Fig. 14(b) and (c), the film was dense, uniform and crack-free, similar to the surface morphologies of the films prepared by spin coating. For one single layer, the thickness was about 10 μm. This is much thicker than the thickness obtained in the spin-coated films. The temperature dependence dielectric constant and loss tangent, together with the tunability of dielectric constant of this thick film are shown in Figure 15. A broad and diffusive peak with the maximum dielectric constant of about 750 was observed. The loss tangent was below 0.01 at room temperature and the tunability was about 33% at 20 kV/cm. The film showed a larger dielectric constant and a slightly better tenability as compared to films prepared by spin coating.

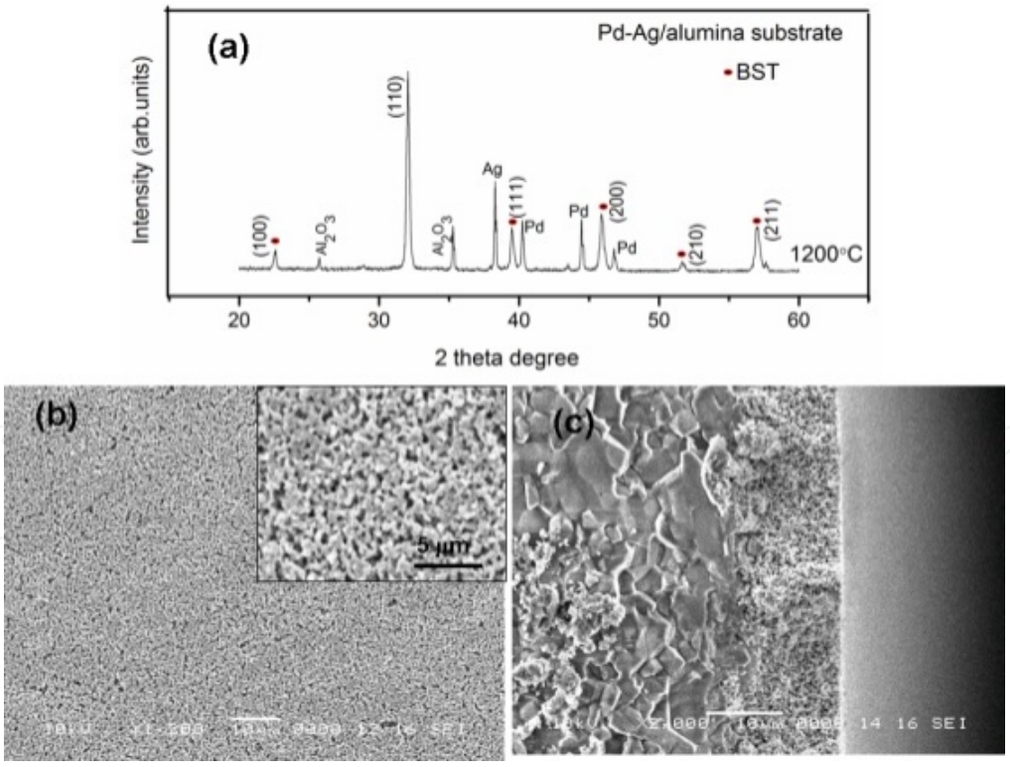

Figure 14. The BST thick films deposited on Pd-Ag/alumina substrate by screen-printing sintered at 1200°C: (a) the XRD pattern; (b) the surface, together with (c) the cross-section micrographs indicating the thickness of about 10 μm. Inset shows the magnified surface picture.

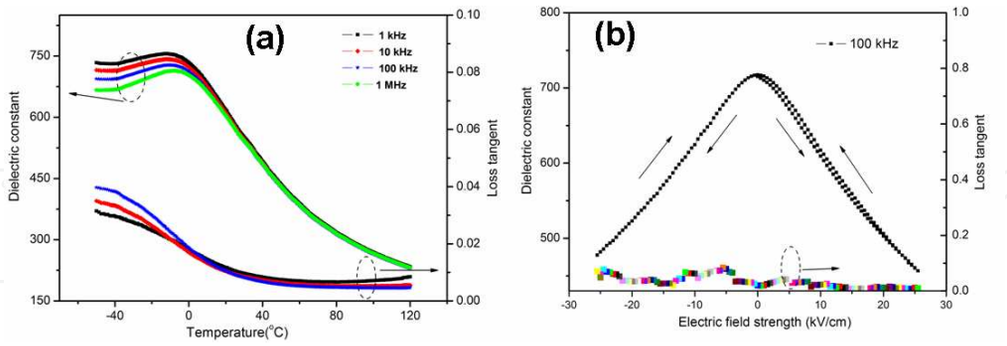

Figure 15. (a) Temperature dependence dielectric constant and loss tangent, and (b) the tuning behavior of dielectric constant of fine-grained BST ceramic at 10 kHz and room temperature under dc bias voltage.

While, Figure 16(a) shows the surface morphology of the BST thick film fabricated from ceramic slurry, which was prepared by combining nano-sized and micron-sized BST powders as the filler in the BST sol precursor matrix. Inset of Fig. 16(a) shows the magnified surface profile. The film was screen-printed on Pd-Ag/alumina substrate and annealed at 1200°C. It is interesting to find that inhomogeneous concrete-like structure, in which big grains in the diameter around ten or tens of micrometers (stones in concrete) and medium grains in the range of micrometer or sub-micrometers (sands in concrete) were adhered by gel derived substance. The dielectric constant was found to be about 1800 with a loss tangent slightly below 0.02 at 10 kHz at room temperature. These values were higher than those values shown in Fig. 15, but close to those values obtained in bulk ceramics formed by conventional solid-state technology. However, the detailed characteristics of the novel concrete-like structures still need to be further studied in future work.

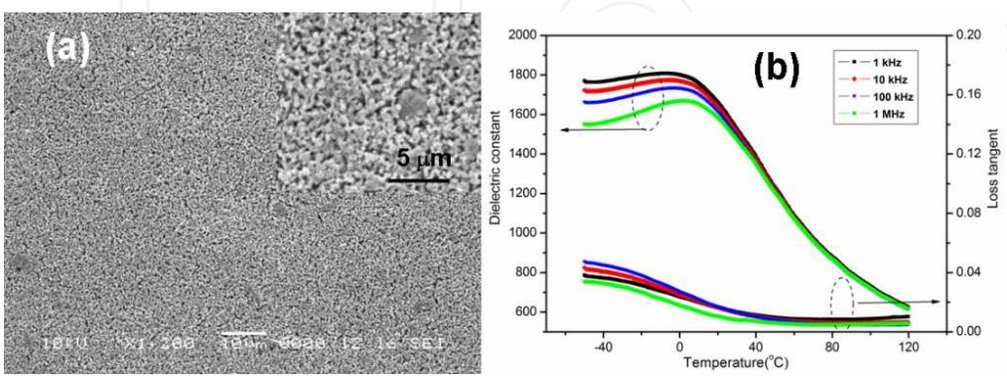

Figure 16. (a) Surface micrograph and (b) temperature dependence dielectric constant as well as loss tangent of the BST thick film which was prepared by combining nano- and micron-sized BST powders as filler and screen-printing on Pd-Ag/alumina substrate. The film was annealed at 1200°C. Inset shows the magnified surface picture.

http://dx.doi.org/10.5772/53255

3.3. Ferroelectric fine-grained glass-ceramic composites

Apart from BST ceramics composites, this modified hybrid process was employed to produce fine-grained $Pb(Zr,Ti)O_3$-based glass-ceramic composites. In general, fine ferroelectric glass-ceramics with high-crystalline phase content are desirable for better dielectric properties; however, the content is quite limited by using conventional melting/quenching glass-ceramics technique [26], because of the high volatility of the lead and the high melting temperature of the zirconium. Besides, zirconium is simply not soluble in many types of glass. On the other hand, in ferroelectric glass-ceramics derived from conventional sol–gel process, aggregation of ultrafine powders and formation of secondary phases are still difficult to be overcome [23]. Therefore, we applied the hybrid processing to fabricate the fine-grained $Pb(Zr,Ti)O_3$-based ferroelectric glass-ceramic composites at relatively low sintering temperatures of below 900°C. A dense, homogeneous, and fine-grained ferroelectric glass-ceramic composite were achieved successfully.

3.3.1. Sintering behavior

Nano-sized $Pb(Zr_{0.53}Ti_{0.47})O_3$ (PZT) powder was prepared via a polymer-assisted sol–gel method sintered at 800°C for 2h [17]. Alternatively, $PbO\text{-}B_2O_3\text{-}SiO_2$ (PBS) ternary phase with molar ratio of 2:2:1 was selected and used to form the PBS sol precursor. Then, PBS sol precursor was poured into glass vessel and kept at room temperature for three days to form a gel. The translucent gel was then dried at 120°C for 10 h. The dried gel was dissolved in ethanol together with the nano-sized PZT powder. The mixture was then mixed thoroughly to form $Pb(Zr_{0.53}Ti_{0.47})O_3$–$PbO\text{-}B_2O_3\text{-}SiO_2$ (PZT–PBS) powder-solution suspension/slurry (gel solution) by conventional ball milling for 2 h. The mass ratio of the PBS dried gel powder ($W_{gel}(wt\%)$) to the nano-sized PZT powder was in the range of 3–30 wt%. The final slurry was dried at 120°C, calcined at 450°C for 2 h, and granulated to obtain PZT–PBS ceramic powders. The powders were uniaxially pressed into disk pellets with a diameter of 13 mm and a thickness of about 0.7–1 mm at a pressure of 4 MPa in a stainless steel die. All the pressed pellets were finally sintered at 900°C for 4 h in air atmosphere, except for 30 wt% sample which was sintered at 850°C.

3.3.2. Microstructure and properties

The XRD patterns of (a) PBS gel powder, (b) nano-sized PZT powder, (c)-(f) PZT–PBS glass-ceramics composites with various glass-gel contents are shown in Fig. 17. For PBS-glass system, no sharp peaks were detected indicating the amorphous nature of the PBS dried gel powder. For nano-sized PZT powder calcined at 800°C, the XRD pattern exhibited a pure perovskite PZT structure. In Figs. 17(c)–(f), the XRD patterns indicated the presence of highly pure and crystalline pervoskite PZT structure in the PZT–PBS glass-ceramics. No intermediate or interfacial as well as impurity phases were observed in all the samples, even for the ceramic with 30 wt% PBS gel content. These results indicated the success in synthesizing PZT–PBS ceramic composites using the modified hybrid processing route. As expected, with increasing wt% of glass gel content, the peak intensity was slightly diminished.

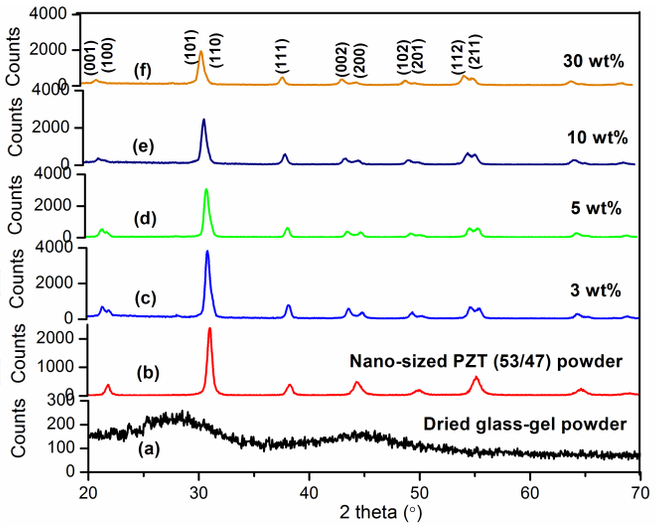

Figure 17. XRD patterns of PBS gel powder (a) dried at 120°C; (b) nano-sized PZT powder calcined at 800°C, together with (c)–(f) the glass-ceramic composites with different glass-gel additions.

The surface and cross-sectional morphologies of a representative sample of 5 wt% glass-gel content are shown in Figure 18. In Fig. 18(a), a dense, homogeneous and well-developed microstructure was obtained at low-firing temperature with a relative density of about 94% theoretical density. Moreover, it is also observed that the grain size of the PZT phases was about 1–2 μm. In Fig. 18(b), the cross-sectional SEM micrograph revealed a mixture of inter- and trans-granular fracture in the glass phase. The EDS analysis showed that the composition of the crystal grain (mark 2) contained only Pb, Ti, Zr and O elements; while for the grain boundary (mark 1), besides Pb, Ti, Zr and O elements, some Si element was detected. The minor amount of Si composition (in *Italics*) shown in the inset of Fig. 18(d) was negligible due to the error of the EDS detector (approximately ±5 at.%). On the basis of our results, we demonstrate that the modified hybrid process proposed in this study (i.e., gel solution in place of the sol precursor) can concisely control the amount of the crystalline phase content employed in the matrix. This new processing technique provides an easy, flexible, and reproducible feature, and should be extensively used in screen-printing, tape-casting or even in traditional ceramics and composites process to reduce the processing temperature.

Figure 19 shows the dielectric constant as a function of temperature for a typical 5 wt% sample at four different frequencies (1 kHz, 10kHz, 100 kHz and 1 MHz). The inset shows the corresponding temperature dependence loss tangents. The room-temperature dielectric constant was about 920 with a loss tangent of about 0.02. As the temperature increased, both the dielectric constant and the loss tangent increased. At about 400°C, the dielectric constant decreased with increasing temperature for different frequencies, except 1 kHz i.e. the dielectric constant of the sample at about 400°C did not drop with increasing temperature at 1 kHz. Thus, the dielectric spectra exhibited a characteristic dispersion at 400°C, namely, the Curie temperature. This indicates that the glass-ceramic composite had a strong tendency of diffusion phase transition. This diffused peak may be owing to the fine structure and the glass-ceramics containing PbO-B_2O_3-SiO_2 continuous matrix [27]. The apparent increase in

http://dx.doi.org/10.5772/53255

dielectric constant at elevated temperature was probably due to increase loss in this temperature range. This trend is consistent with the fact that PZT crystals, surrounded by a glassy matrix, have a higher electrical conductivity at higher temperature. In amorphous materials, the ease of polarizability, and hence dielectric constant, increases with temperature because of their relatively weak bonding structure. Correspondingly, as shown in inset of Fig. 19, the loss tangent increased markedly as the measuring temperature was increased above the Curie temperature.

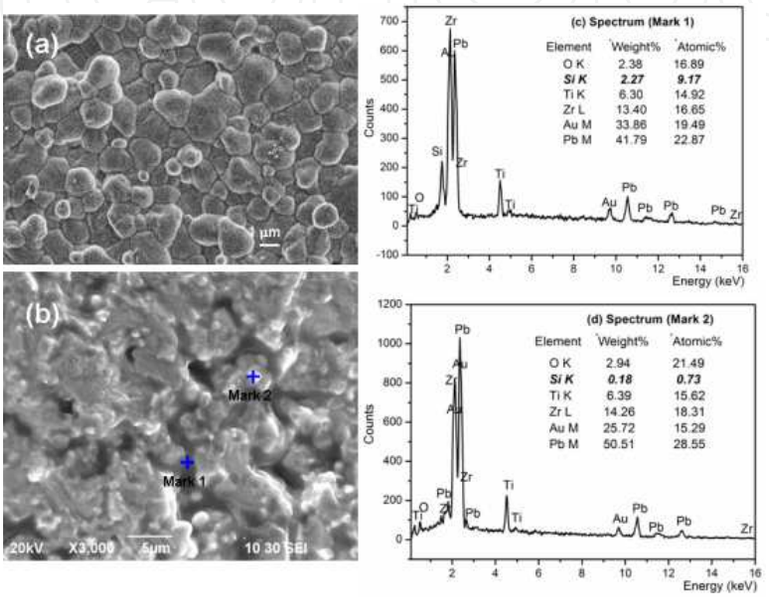

Figure 18. Surface and cross-sectional micrographs of a representative sample with 5 wt% glass-gel content, together with EDS analyses at two spots.

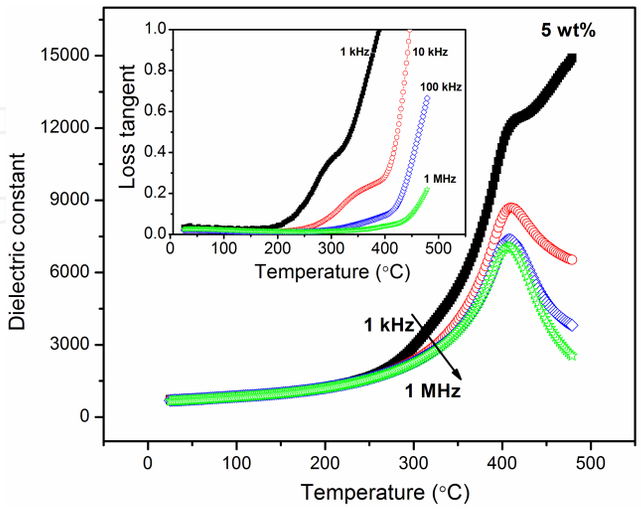

Figure 19. Temperature dependence dielectric constant for a typical 5 wt% sample at 1 kHz–1 MHz. Inset shows the loss tangent as a function of temperature.

Figure 20 shows the room temperature ferroelectric hysteresis loop ($P-E$) for a typical sample with 5 wt% glass-gel content at 100 Hz. The loop showed reasonable ferroelectricity of the embedded PZT (53/47) crystallites, demonstrating a high volume fraction of PZT phase existed in the sample. The measured P_s, P_r and E_c was 21.9 μC/cm^2, 10.8 μC/cm^2 and 2.19 kV/mm, respectively. These results demonstrate that these fine-grained glass-ceramics have a high application potential for micro-electronics.

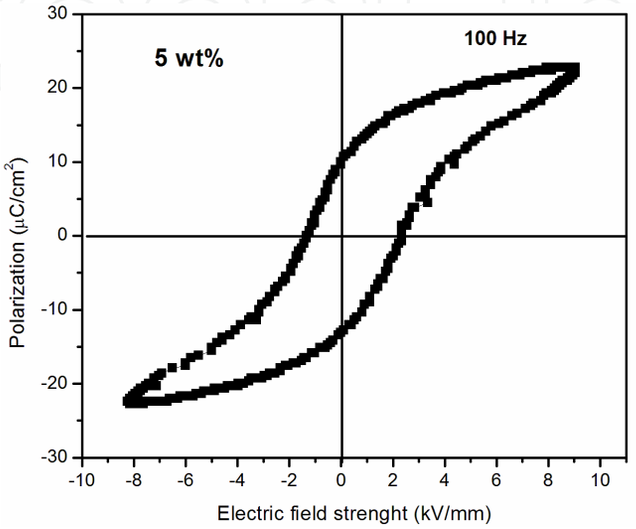

Figure 20. Ferroelectric hysteresis loop of a representative sample with 5 wt% glass-gel content at 100 Hz at room temperature.

3.4. Multiferroic magnetoelectric fine-grained ceramic composites

Following the general tendency of the microelectronic industry towards miniaturization and integration, it is of paramount important to find materials with best properties in small volume and possess more functions in the same structure. Multiferroic materials, which combine two or more primary ferroic orders such as ferromagnetic and ferroelectric orders [28], have attracted considerable research activity in recent years not only because they have the properties of both parental compounds, but also because they show multifunctionality caused by the coupling between the orders [19]. In here, the modified hybrid process as introduced above was employed to prepare the fine-grained multiferroic $Pb(Zr_{0.53}Ti_{0.47})O_3$-$(Ni_{0.5}Zn_{0.5})Fe_2O_4$ (PZT-NZFO) ceramic composites at a low sintering temperature of 900°C.

3.4.1. Sintering behavior

NZFO powder was prepared by a conventional solid-state process. Fe_2O_3, NiO, and ZnO powders were first mixed using conventional ball milling. After calcinating at 1000°C for 2 h, submicron-sized NZFO powder with an average size of 100-500 nm was obtained. Then, the calcined nano-sized PZT powder coated with glassy phase as described in section 3.3.1

http://dx.doi.org/10.5772/53255

was mixed with the NZFO powder by ball milling for 2 h. The resulting ceramic slurry was dried at 150°C for 10 h. The granulated powder was uniaxially pressed into disk (13 mm diameter, 0.50.7 mm thickness) at a pressure of 4 MPa in a stainless steel die. All the specimens were finally sintered in air at 900°C for 4 h. In the present work, wt% ratios of NZFO powder and glass coated nano-sized PZT particulates of 10/90, 15/85, 25/75, 50/50 and 60/40 were adopted (denoted as 10 wt%, 15 wt%, 25 wt%, 50 wt% and 60 wt% composites).

3.4.2. Microstructure and properties

Figure 21 shows the XRD patterns of PZT-NZFO composites at various mixing ratios. In Fig. 21(a), the diffraction pattern of NZFO powder calcined at 1000°C demonstrated a pure and crystalline Ni-Zn ferrite with spinel structure. For nano-sized PZT powder coated by glass and calcined at 450°C [Fig. 21(b)], all the peaks exhibited the presence of pure PZT phase with a perovskite structure. For the composites with 10, 15, 25, 50 and 60 wt% of ferrite contents [Figs. 21(c)-(g)], all the peaks were identified distinctly as either from ferroelectric (PZT) or ferrimagnetic (Ni-Zn ferrite) phases. Thereby, the preparation of a composite containing both ferroelectric and ferrimagnetic phases was successful.

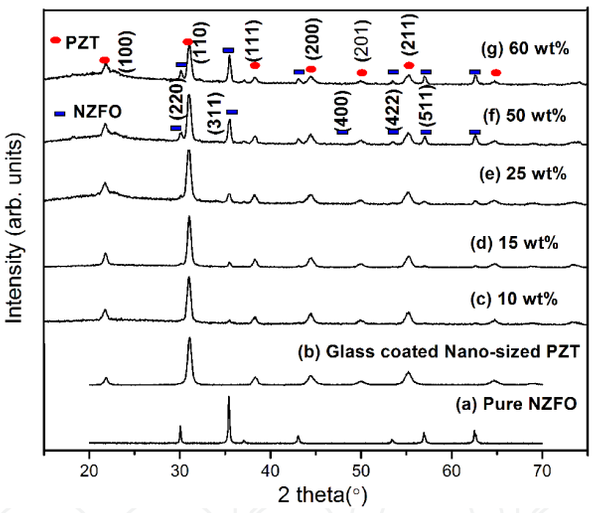

Figure 21. XRD patterns of the PZT-NZFO composite ceramics with various amount of NZFO phase contents sintered at 900°C for 4 h.

Figure 22 shows the surface morphologies of three selected composites with different ferrite contents: (a) 15 wt%, (b) 25 wt%, and (c) 50 wt%. General speaking, the surface of the composites were dense and homogeneous. Well-developed fine grains were observed with a good mixture of the two phases in the ceramics at low firing temperature. The EDX results suggested that grains of average size of 1- 2 μm were the PZT phase and those of size below 500 nm were the NZFO phase. It was clearly seen that the grain size of NZFO phase (about 100–500 nm) remained unchanged in all the samples. Here, well-crystallized NZFO powders were used as template (i.e. 3-0 connectivity pattern) for the in-situ preparation of the composites, the subsequent sintering for promoting the PZT grain growth practically did not

change the crystallization of the NZFO component. Besides, the grain size of PZT phase in the ceramics was well-controlled and possessed a narrow size distribution with no formation of large grain. This means that excessive grain growth could be restrained by the modified hybrid process. For various compositions of PZT-NZFO ceramics sintered at same temperature, the proportion of the two phases determined from the relative peak intensity ratios of the parent phases roughly agreed with the nominal ones [Fig. 21(c)-(g)].

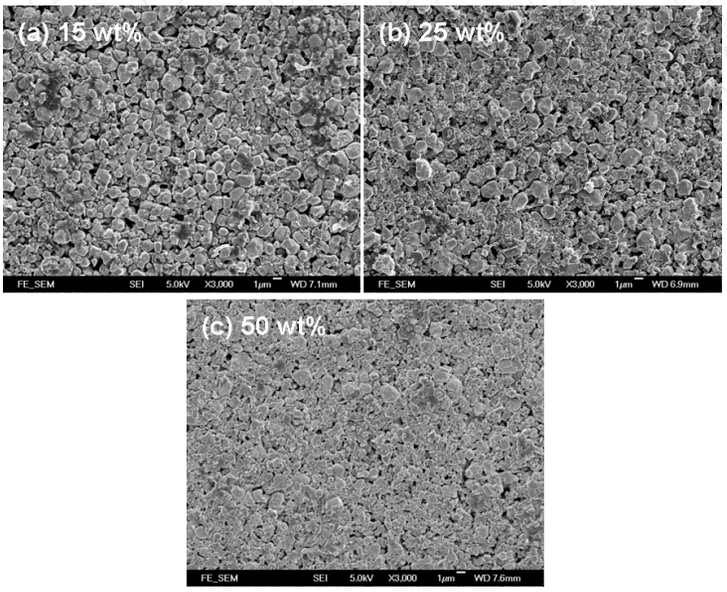

Figure 22. SEM surface micrographs of the composite ceramic with various amounts of NZFO content.

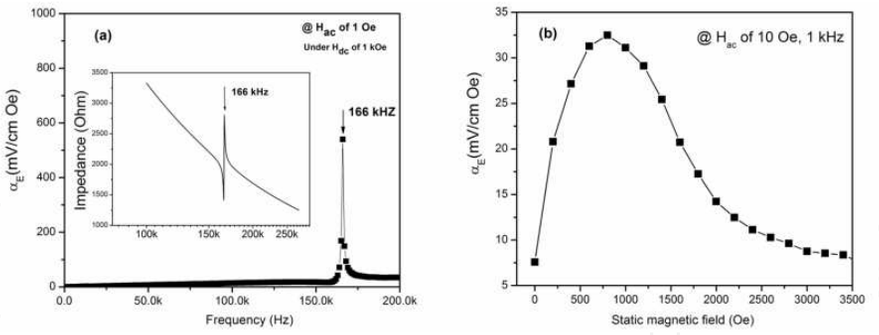

Figure 23. (a) Frequency dependence α_E under H_{dc}=1 kOe and H_{ac}=1 Oe, (b) the dc bias magnetic field dependence α_E under an ac magnetic input signal at 1 kHz and 10 Oe amplitude. The inset in (a) shows the impedance as a function of frequency in a poled 15 wt% composite.

Magnetoelectric (ME) coupling effect in the 15 wt% composite was studied by measuring the voltage response of the sample exposed to alternating and constant (bias) magnetic field as shown in Figure 23. In Fig. 23(a), a dramatic gain of up to 0.537 $Vcm^{-1}Oe^{-1}$ in the vicinity of electromechanical resonance was found. In Fig. 23(b), with an increase in dc bias magnetic field, α_E increased to a maximum value of about 33 $mVcm^{-1}Oe^{-1}$ at 1 kOe and then drop-

ped with increasing dc bias field. It remained nearly constant beyond 3 kOe. We attribute the high α_E to high quality of fine-grained microstructure obtained by the modified hybrid processing at low firing temperature which avoids undesired phases and interphase diffusion of the constitutional atoms caused by the high-temperature sintering in conventional solid-state process. Furthermore, this low firing temperature lessens the thermal expansion mismatch due to the different sintering behavior between the constituent ferroelectric and ferrimagnetic phases. It also reduces the formation of microcracks and pores in the composites. Therefore, the ME response of the composite ceramics can be enhanced by transferring elastic strains fully when the components are in good contact. In this current work, the enhanced ME coupling in the fine-grained composite might find promising applications as high-frequency magnetic field sensors, transducers and magnetic field tunable microwave signal processors.

4. Summary

In this chapter, fine electronic ceramics, such as tunable microwave bulk barium-strontium titanate $(Ba_{0.6}Sr_{0.4})TiO_3$ (BST) ceramics, thick BST films, BST-MgO bulk ceramics, and ferroelectric $Pb(Zr_{0.53}Ti_{0.47})$ (PZT)−based glass-ceramics, as well as multiferroic $Pb(Zr_{0.53}Ti_{0.47})$-$(Ni_{0.5}Zn_{0.5})Fe_2O_4$ (PZT-NZFO) ceramic composites, have been successfully prepared by either hybrid or modified hybrid process at low sintering temperatures. For bulk BST ceramics, a well-densified and homogeneous microstructure was obtained at a sintering temperature of 1200°C, which was 200°C lower than that of the conventional solid-state process. The BST thick films were deposited on various substrates including Pt, Ag/alumina and Pd-Ag/alumina by spin-coating or screen-printing methods. High quality thick films were fabricated at annealing temperatures ranging between 600~1200°C. In addition, dense, homogeneous and well-sintered BST-MgO ceramics with grain size of 300 nm−2 μm were produced at sintering temperature < 1300°C, 100−200°C lower than that of the conventional solid-state ceramic process. At the same time, PZT based ferroelectric glass-ceramics were investigated. Dense and well-developed glass ceramic composites with a grain size below 2 μm were produced at a relatively low sintering temperature of 900°C by a modified hybrid process, and the apparent ferroelectric hysteresis loop demonstrated the high volume fraction of ferroelectric phase in the glass-ceramic composite, which overcome the drawback of both conventional melting/quenching glass-ceramic technology and sol-gel route. Finally, the modified hybrid process was introduced to prepare multiferroic magnetoelectric PZT-NZFO ceramic composite at a low sintering temperature of 900°C. Dense, well-developed and homogeneous microstructures were obtained with a well-controlled grain size and good mixing of the two phases in the ceramics. On the basis of our studies, we demonstrate that either the hybrid or the modified hybrid ceramic processing technology is a very promising new technology for fabrication of ceramics as well as composites. We consider that this approach should also be useful for almost all the ceramic materials and devices, realizing the dream of retaining a fine or ultra-fine grain size in fully sintered products at relatively low firing temperature by a simple, flexible and reproducible processing.

Acknowledgement

This work was supported by the Hong Kong Polytechnic University under Grant No. GYJ72.

Author details

Hongfang Zhang[1*], Chee-leung Mak[2], Helen Lai-Wa Chan[2] and Xi Yao[3]

*Address all correspondence to: zhf057@gmail.com

1 Department of Physics , Suzhou University of Science and Technology, Suzhou, China

2 Department of Applied Physics, The Hong Kong Polytechnic University, Hung Hom, Kowloon, Hong Kong

3 Functional Materials Research Laboratory, Tongji University, Shanghai, China

References

[1] Bell AJ. Ferroelectrics: The Role of Ceramic Science and Engineering. Journal of The European Ceramic Society 2008; 28 (7) 1307-1317.

[2] Setter N. and Waser R. Electroceramic Materials. Acta Materialia 2000; 48 (1) 151-178.

[3] Petrov VM, Bichurin MI, Laletin VM, Paddubnaya MN and Srinivasan G. Modeling of Magnetoelectric Effects in Ferromagnetic/Piezoelectric Bulk Composites. In: Fiebig M., Eremenko VV, Chupis IE (eds) MEIPIC-5: Magnetoelectric Interaction Phenomena in Crystals: proceeding of the fifth International Meeting on Magnetoelectric Interaction Phenomena in Crystals, NATO Advanced Research Workshop (ARW), 21-24 September 2003, Sudak, Ukraine.

[4] Kokubo T and Tashiro M. Dielectric Properties of Fine-Grained $PbTiO_3$ Crystals Precipitated in a Glass. Journal of Non-Crystal Solids 1973; 13(2) 328-40.

[5] Beall GH, Flats B, Pinckney LR. US Patent No. 5,491,116, February 13, 1996.

[6] Cai H, Gui Z, Li L. Low-sintering Composite Multilayer Ceramic Capacitors with X7R Specification. Materials Science and Engineering: B 2001; 83(1) 137-141.

[7] Newnham RE, Bowen LJ, Klicker KA. Cross LE., Composite Piezoelectric Transducers. Materials & Design 1980; 2(2) 93-106.

[8] Yang WH, Yu SH, Sun R, Du RX. Nano- and Microsize effect of CCTO Fillers on the Dielectric Behavior of CCTO/PVDF Composites. Acta Materialia 2011; 59(14) 5593-5602.

[9] PFISTERER INTERNATIONAL AG. Germany: Composite Insulators for High Voltage Applications. http://www.pfisterer.com

[10] Ruschau GR, Newnham RE, Runt J. Smith BE. 0–3 Ceramic/Polymer Composite Chemical Sensors. Sensors and Actuators 1989; 20 (3) 269-275.

[11] Dislich H. Glassy and Crystalline Systems from Gels: Chemical Basis and Technical Application. Journal of Non-Crystal Solid 1984; 63(1-2) 237-241.

[12] Muralt P. Ferroelectric Thin Films for Micro-sensors and Actuators: a review. Journal of Micromechanics and Microengineering 2000; 10(2) 136-146.

[13] Park GT, Choi JJ, Park CS, Lee JW, and Kim HE. Piezoelectric and Ferroelectric Properties of 1-μm-thick Lead Zirconate Titanate Film Fabricated by a Double-Spin-Coating Process. Appled Physic Letter 2004; 1794354 (85) 2322-2325.

[14] Bruchhaus R, Pitzer D, Primig R, Schreiter M, Wersing W. Sputtering of PZT Thin Films for Surface Micromachined IR-detector Arrays. Integrated Ferroelectrics 1999; 25(1-4) 1-11.

[15] Scott JF. High-dielectric Constant Thin Films for Dynamic Random Access Memories (DRAM). Annual Review of Materials Research 1998; 28: 79-100.

[16] [16]Mukhortov VM, Masychev SI, Golovko YI, Chub AV, and Mukhortov VM. Application of Nanodimensional Barium-Strontium Titanate Films in Tunable Microwave Devices. Technical Physics 2006; 51(10) 1359-1361.

[17] Zhang HF, Mak CL. Preparation and Characteristics of Fine-grained Ferroelectric Glass-ceramic Composites via a Modified Hybrid Route at Low Temperature Sintering. Journal of Electroceram 2011; 27:126-133.

[18] Zhang HF, Or SW, and Helen Chan WL, Yang F. Formation and Characterization of Three-ply Structured Multiferroic $Sm_{0.88}Nd_{0.12}Fe_{1.93}$–$Pb(Zr_{0.53}Ti_{0.47})O_3$ Ceramic Composites via a Solid Solution Process. Journal of European Ceramic Society 2011; 31(9) 1753-1761.

[19] Zhang HF, Or SW, and Helen Chan WL. Multiferroic Properties of $Ni_{0.5}Zn_{0.5}Fe_2O_4$–$Pb(Zr_{0.53}Ti_{0.47})TiO_3$ Ceramic Composites. Journal of Applied Physics 2008; 104: 104109.

[20] Zhang HF, Yao X, Zhang LY. Microstructure and Dielectric Properties of Barium Strontium Titanate Thick Films and Ceramics with a Concrete-like structure. Journal of American Ceramic Society 2007; 90 (8) 2333-2340.

[21] Zhang HF, Or SW, and Helen Chan WL. Synthesis of Fine-crystalline $Ba_{0.6}Sr_{0.4}TiO_3$–MgO Ceramics by Novel Hybrid Processing Route. Journal of Physics and Chemistry of Solids 2009; 70(8) 1218-1222.

[22] Zhang HF, Zhang LY, Yao X. Fabrication and Electrical Properties of Barium Strontium Titanate Thick Films by Modified Sol–Gel Method. Journal of Electroceramics 2008; 21(1-4) 503-507.

[23] Dislich H, Hinz P. History and Principles of The Sol-gel Process, and Some New Multicomponent Oxide Coatings. Journal of Non-Crystalline Solids 1982; 48 (1)11-16.

[24] Chang W, Sengupta L. MgO-mixed Ba0.6Sr0.4TiO3 Bulk Ceramics and Thin Films for Tunable Microwave Applications. Journal of Applied Physics 2002; 92(7) 3941.

[25] Sengupta L, Ngo E, Stowell S, O'Day M, Lancto R. US Patent No 5,427,988, 1995.

[26] Yao K, Zhang LY, Yao X, Zhu WG. Controlled Crystallization in Lead Zirconate Titanate Glass-Ceramics Prepared by the Sol–Gel Process. Journal of American Ceramic Society 1998; 81 (6) 1571-76.

[27] Zhai JW, Yao X & Zhang LY. The High Frequency Properties and Crystallization of $PbTiO_3$ Glass-Ceramics by Sol-Gel Process. Journal of Electroceramics 2000; 5(3) 211-216.

[28] Schmid, H. Multi-ferroic magnetoelectrics. Ferroelectrics 1994; 162 (1) 317-338.